Analysis of micro-vasculature in whole kidney specimens using Micro-CT

John G. Sled[a,c], Michael Marxen[b,c] and R. Mark Henkelman[a,b,c]

[a]Hospital for Sick Children, Toronto, Canada
[b]Sunnybrook and Women's College Health Sciences Centre, Toronto, Canada
[c]Department of Medical Biophysics, University of Toronto, Toronto, Canada

ABSTRACT

Micro-computed tomography (micro-CT) provides a means for obtaining a detailed three-dimensional description of the structure of micro-vasculature in whole organs. This whole organ description allows for the examination of flow models and self similarity relationships that would otherwise be inaccessible using conventional sampling based descriptions of the micro-vasculature. The number of vessels that compose the micro-vasculature in a whole organ is so large, however, that such analysis is only feasible using automated image processing techniques. In this paper, the segmentation and data representation challenges of such analysis are examined with reference to mouse kidney vasculature. A semi-automated analysis method is described and is applied to a set of mouse kidneys to assess the feasibility and reproducibility of population studies. This analysis includes a new method to separate parallel arterial and venous vessels that are distinct but touching at the resolution of the micro-CT scan. Also described is a new formalism for representing the derived vessel structure that lends itself to regularization. Distributions of arterial and venous structural parameter are presented for six kidneys (three of each) taken from age matched animals of the CD1 strain. These results show a high degree of similarity among specimens and suggest that population studies to examine the influence of subtle disease or genetic factors are feasible.

Keywords: micro-computed tomography, microvasculature, segmentation, parallel vessels, skeletonization, mouse, kidney

1. INTRODUCTION

Three-dimensional structure is an important aspect of the vascularization of tissue in an organ. The cascade of finer and finer branched vessels connecting arteries to capillaries decelerates the blood to a rate that allows exchange of oxygen and metabolites before it is drained away by a merging network of veins. The need to regulate temperature, distribute metabolites, and remove waste while adapting and maintaining the vessel network constrains its design. Moreover the limited energy reserve of tissue necessitates that the system be robust and redundant. A developmental story in which an initial patterning of the vascular system gives way to local factors affecting growth, the accommodation of other simultaneously developing structures, as well as a process of remodelling in response to changing metabolic need also influences the overall pattern. Motivated by a desire to better understand the complex patterning of the microvasculature and the regularities present in its structure, we describe here an approach to analyzing microvascular architecture using a combination of micro-CT and computer analysis.

Past efforts at describing microvascular structure have made use of sampling techniques (eg. serial sections) to derive geometric properties.[1] Using these measurements and concepts of self-similarity, the vascular system has been studied using theoretical and computer modelling approaches.[2–10] While computer models can provide insight, there are a number of limitations. Specifically, most measurement techniques and many of the computer models neglect the three-dimensional nature of the structure. Furthermore, a vessel sampling strategy may not capture the complexity of a structure and may be biased by the observer's selection of features. Moreover, even when the measurement strategy is sound, these average properties may not be sufficient to construct a realistic

Address correspondence to: John G. Sled, Hospital for Sick Children, Mouse Imaging Centre, 555 University Avenue, Toronto, Ontario, M5G 1X8. E-mail: jgsled@sickkids.ca

artificial vasculature from which general properties can be derived. Concepts such as self-similarity may apply in an average sense without being true of every branch in the structure.

To overcome these limitations, we present a methodology to describe vascular structures as a whole by making use of high resolution three-dimensional data sets collected using micro-computed tomography (micro-CT) as pioneered by Ritman and colleagues.[11,12] The data sets used in this study have a resolution of 22 μm[13] thus allowing for a description of the structure which includes all but the finest vessels. Since such data can be acquired rapidly, over the course of a few hours, this approach allows for population studies that would not be feasible using conventional morphometric techniques. The challenge in conducting such studies using micro-CT shifts from one of collecting sufficient data, to that of reducing vast voxelated data sets to geometrical representations that are amenable to analysis.[14] In this paper, we address the problem of constructing useful representations of vascular structure from high resolution CT data.

Consider the three examples of mouse kidney vasculatures from a CD-1 mouse strain (i.e. nearly genetically identical animals) shown in Figure 1. From visual inspection these structures show a great deal of similarity, yet quantifying this similarity in precise terms is difficult. A simple description of the data in Figure 1 is that of venous and arterial branching networks, the basic elements of which are vessel segments. In refining this description, one needs to define the path that a vessel follows in a precise manner so that thousands of segments can be processed in a consistent and largely automated manner. In this paper, the segmentation and data representation challenges of such analysis are examined for the application of this technology to population studies.

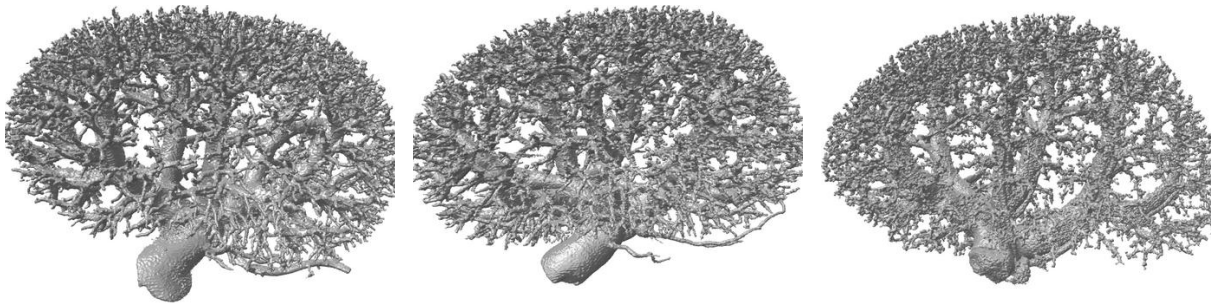

(a) (b) (c)

Figure 1. Surface renderings of three mouse kidney vasculatures from the CD-1 strain. All three are right kidneys visualized with the superior aspect on the left. These are referred to as specimens L1, L2, and L3 in the text.

2. METHODS

2.1. Data acquisition

For these experiments six CD-1 female mice (Charles River Laboratories, Wilmington, MA) age 11-13 weeks were prepared using the procedure summarized here. The animals were anesthetized by interperitoneal injection of ketamine (50 mg/kg) and xylazine (10 mg/kg). Following a 500 unit subcutaneous injection of heparin and a thoracotomy, a solution of heparin (1 unit/ml) and physiologically buffered saline at 37° C injected through the left ventricle and drained from the right atrium was used to replace the blood. This was followed by an infusion of Microfil (Flow Tech Inc., Carver, MA), a silicone rubber compound that for the medium viscosity (MV) preparation has a viscosity initially comparable to blood and that begins to harden 30 minutes after injection. The medium (MV) and high viscosity (HV) preparations, $\sim$ 30 and $\sim$ 400 centipose respectively, consisted of 4 ml of Microfil MV122, 5 ml of either MV or HV diluent and 0.45 ml of curing agent. The kidneys were excised and stored at 4° C in a solution of 10% neutral buffered saline. The infused Microfil was allowed to cure over a period of 12 hours and was the source of contrast in the resulting CT images. All fluids were infused at a constant pressure of 160 mmHg (21.3 kPa).

Three-dimensional CT data sets were acquired for each excised kidney using a MS-8 micro-CT scanner (GE Medical Systems, London, Ontario).[13] With the X-ray source at 80 kVp (mean energy of incident beam: 32 keV), these were acquired in 2.5 hours with 900 views and reconstructed using the Feldkamp algorithm[15] for cone beam CT geometry. This yields 500x800x1000 data blocks of 10 μm voxels (800 Mb of data). To facilitate computation on a 32 bit PC architecture, we applied 2x2 binning of the projection data and reconstructed the datasets using 20 μm isotropic voxels. The computed images show both arterial and venous vessels as highly intense regions against a relatively uniform dark background. A limited amount of contrast agent is also visible in the renal tubules.

2.2. Vessel extraction

All of the CT images were segmented into foreground and background using a simple threshold of between 1350 and 2300 Hounsfield units (HU). These thresholds were chosen based on visual assessment to compensate for differences in the quality of the perfusion of the vessels with contrast agent. Major vessels, which were consistently well perfused, had an intensity of 3000 to 5000 HU. The FWHM of the micro-CT system's plane spread function (PLSF) is 22 μm.[13] For larger vessels, a threshold at half the attenuation of the contrast agent should accurately delineate vessel boundaries. In smaller vessels, comparable in diameter to the PLSF, this threshold under represents their diameter. Assuming a Gaussian PLSF, the range of thresholds used in this analysis corresponds to a maximum bias in diameter estimates of 16 μm for large vessels (i.e. by less than a voxel).

Within the region determined by simple thresholding, the vascular structure was separated from other elements of the images using seeded region growing.[16] A difficulty with segmentation based on intensity thresholds is that a single voxel within the vessel that is unusually dark due to noise or artifact can substantially alter the topology of the resulting segmented region. This was addressed in this work by identifying and filling holes in the (26-neighbour connected) segmented region.

The result of the segmentation procedure is a binary map of the connected vascular structure present in the CT data. To reduce this segmented vessel region to a network of connected vessels, we applied a modified form of the skeletonization procedure described in.[17] Briefly, this procedure allows a skeleton consisting of connected curved paths to be derived from the distance transform and distance coding of a binary object. The former is defined at any point as the distance to the nearest object edge. The latter is similarly defined as the shortest distance at any point along a path through the object back to a seed point, which for this work was placed at the base of the renal vein. Lengths are approximated in the implementation by the distance along a path passing through the centres of adjacent voxels. These so called voxel-coded or chamfer distances are computed using integer approximations of the distance between face, edge, and vertex adjacent voxels. For the distance transform these distances are approximated as 3, 4, and 5 respectively, whereas for the distance coding the values 1, 2, and 3 are used.

Collections of adjacent points equidistant from the seed point are termed clusters. A sequence of clusters increasingly distant from the seed point can be thought of as a propagating wave travelling down a vessel. These clusters and the directions of propagation are illustrated schematically for a branching vessel in Figure 2a. For each cluster, the center is taken as the voxel within the cluster having the maximum distance transform value that is nearest to the geometrical centre of the cluster (see Figure 2b). Linking together adjacent clusters yields a skeleton of the object as shown in Figure 2c. For this work, clusters were considered adjacent if they shared a voxel face (i.e. 6-connected).

A difficulty with the approach described so far, and with skeletonization procedures in general, arises when an artery and vein travel in parallel and touch periodically. This occurs frequently in mammalian vascular systems and is a mechanism for heat exchange in the peripheral circulation.[18,19] In these instances, what is desired from the skeletonization algorithm is not the curved paths approximating the medial surface that the algorithm is designed to produce and which reflects the topology of the segmented region, but instead the skeletonization of the artery as though the vein were not present and vise versa. This situation is illustrated schematically in Figure 2d.

Touching vessels are separated by analyzing the values of the distance transform within each cluster. Although clusters are not strictly restricted by the algorithm to be planar, they can be thought of as cross-sections of the

given vessel or touching vessels. The distance transform values projected onto a cluster have a maximum at the centre of the largest transected vessel. If a second vessel can be resolved from the cross-section then a second distinct local maximum will be present. Clusters with more than one local maximum are subdivided into smaller clusters (see Figure 2e) using the distance transform values as a guide. Specifically a voxel in a cluster is associated with a particular local maximum if a gradient ascent from that point on the distance transform leads to the given local maximum.

Following subdivision, adjacent subclusters are linked to form a skeleton of the combined system of vessels taking into account that most connections crossing over from one row of subclusters to another are unwanted (see Figure 2f). The division procedure has the side effect of improving the location of branch points as illustrated by the difference between Figures 2c and 2f. Following the division step, the vessel network is represented abstractly as a graph with clusters corresponding to nodes and links determined by cluster adjacency as graph edges.

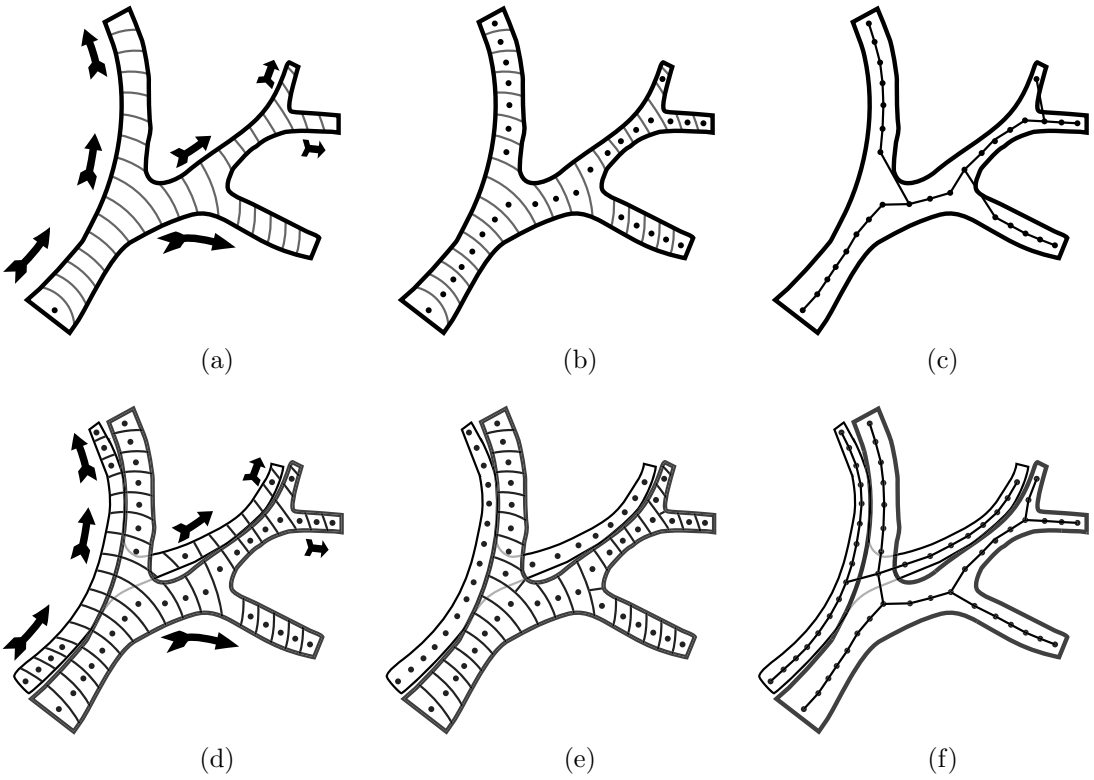

Figure 2. An illustration of the clustering and skeletonization procedure. (a) clusters of voxels equidistant from the seed point shown at the bottom left. (b) cluster centres determined from the maximum of the distance transform. (c) vessel network created by connection of adjacent clusters. (d) clusters determined for parallel partly touching vessels. (e) clusters determined by division of clusters with multiple distance transform maxima. (f) vessel network derived for the divided clusters following deletion of crossover connections.

Figure 3a shows a few major vessels that have been manually segmented from a micro-CT scan of a whole kidney with the renal artery and vein beginning at the base of this structure as indicated. We use this object to illustrate the segmentation of veins. With a seed point placed at the base of the renal vein, the skeletonization procedure produces the network shown in Figure 3b. The resulting network shows both the venous and arterial branches as well as a number of spurious interconnections between the two. At finer scales, however, the arteries cannot be distinguished from the larger adjacent veins. Hence we proceed by deleting the arterial side of the structure using a semiautomated procedure.

A feature of the skeletonization algorithm which is not evident in Figure 3b, but which is illustrated in 2e is the distance between the centres of connected clusters. In particular, as one follows a vessel the connections

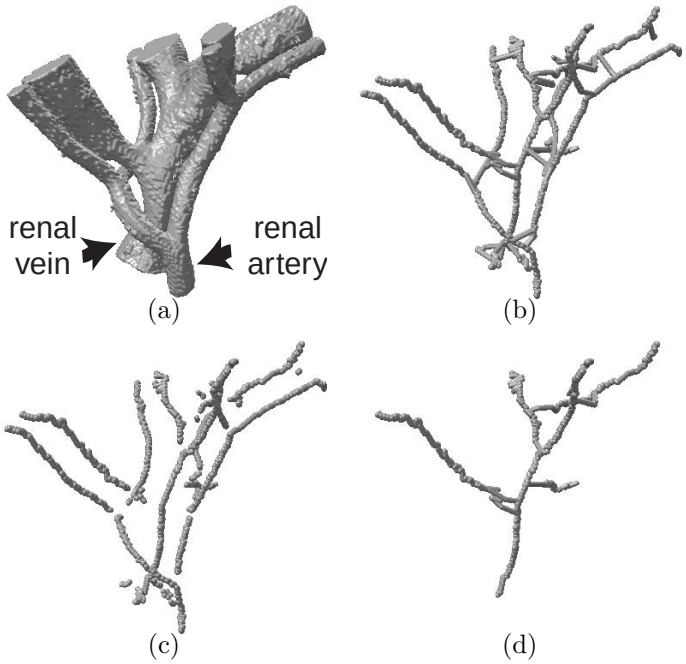

Figure 3. (a) a pair of parallel branching vessels identified by manual segmentation. (b) vessel skeleton derived for the structure in (a). (c) connected vessel components after deletion of connections between clusters longer than 75 μm. (d) structure in (b) following deletion of the components identified as arterial in (c).

between cluster centres tend to be short whereas the connections at branch points or spurious connections between parallel vessels tend to be long. Given that the separation of arteries and veins is only possible for large vessels, we proceed by initially severing all connections greater than 75 μm in length. The connected components that remain following this step are shown for the example case in Figure 3c. Those components belonging to the arterial tree are identified manually using an interactive 3D visualization package.[20] All arterial nodes in the identified components are then deleted from the original skeletonization (Figure 3b) to produce the result shown in Figure 3d. This structure is taken to be the skeleton of the venous vessel network. Note that while the choice of 75 μm is arbitrary, the large difference in the relative diameter of adjacent arteries and veins means that vessel pairs with centres closer than 75 μm cannot be resolved due to the resolution of the data.

Noise in the original CT data, surface imperfections on the vessel walls, and fine structure beyond the resolution of the scanner can produce fine hair-like structure along the skeleton of a vessel segment. This is a common difficulty with skeletonization which we addressed by removing branches consisting of only a few nodes (three or less). Spurious cycles in the vessel graph can also arise from the same sources. Cycles were removed by deleting the graph edge furthest from the base of the vessel tree. While some cycles could be true anatomical features, visual inspection suggested that this was not the case in any of the samples examined. In organs such as the brain where true cycles are anticipated or in pathological conditions, a more refined procedure for deleting cycles would be required.

2.3. Vessel representation

A simplified representation of a vessel tree is obtained by distinguishing graph nodes with more than two edges as vessel junctions and describing the connecting elements between these junctions as vessel segments. While this representation facilitates such tasks as counting of terminal nodes, it does not lend itself to a robust description of the vessel structure. In view of these limitations we represent the vessel tree in a form which we term a principal vessel graph (PVG).

Using the terminology that the node at the base of the vessel tree is proximal, the principal vessel graph is developed as follows. Starting from base of the graph, distal vessel segments are added to the principal vessel by choosing at each junction the vessel segment with the largest diameter (at the end approaching the junction). This process continues until a terminal node in the vessel graph is reached. This procedure is repeated for each branch attached to the principal vessel and each branch of those branches until all of the vessel segments are consumed. Figure 4a shows an example of a principal vessel in which all of the clusters corresponding to the vessel have been rendered as a solid.

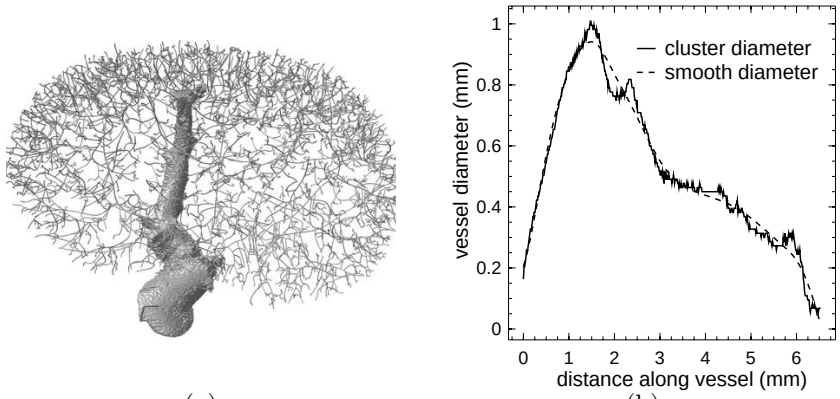

(a) (b)

Figure 4. Modelling the principal vessel. (a) A smooth principal vessel graph with the clusters corresponding to the principal vessel rendered as a solid. (b) A graph of cluster diameter and its smooth approximation by cubic B-splines along the length of the principal vessel.

The PVG decomposition means that for each junction one of the branches is the distal continuation of the given vessel while the other branch is treat separately for the purposes of regularization. This distinction is based on the vessel segment radii approaching the junction estimated as the distance transform value for the cluster centre adjacent to the junction. Using this metric to define vessel diameter is equivalent to determining the largest sphere that can be inscribed within the given vessel at that location.

The use of a PVG allows for a smooth representation of the vessels. For each vessel in the PVG, cubic B-splines with optimally distributed knot points[21] were used to approximate the trajectory of the vessel as a parameterized curve. Similarly, the diameter of the vessel was approximated by cubic B-splines along the length of that curve (see Figure 4b). Note that the distance transform values tend to oscillate and have maxima at bifurcation points. In both cases, the approximation was based on one measurement per cluster and the curves were parameterized by ordinal numbering of the clusters. The spline implementation[22] imposes regularity by minimizing the discontinuities in the 3rd derivative while maintaining an upper bound on the sum-of-squares fitting error. This upper bound was chosen to give a maximum mean fitting error of 55 μm for vessel trajectories and 32 μm for vessel diameters. For vessels that join with a parent vessel, the endpoint of the spline is constrained to join the parent vessel at the bifurcation point on the smooth version of the parent vessel. As a consequence, the smoothing approximation must be applied recursively to the PVG starting from the root.

2.4. Derivation of structural properties

Given the parameterized representation of the vessel tree, a variety of geometric properties can be derived. The geometric properties that we used in our analysis were vessel diameters and vessel lengths. For a given bifurcation, the parent vessel segment is denoted 0 and the two daughter segments 1 and 2 respectively, where 1 is of larger diameter than 2. A vessel segment is the portion of a vessel connecting one bifurcation to another or to an end point. The diameter of the vessel segments forming a bifurcation, denoted d_0, d_1, and d_2, are computed as the mean smooth diameter along those segments. In this work we also used bifurcation asymmetry γ defined as

$$\gamma = d_2/d_1. \tag{1}$$

For the purposes of examining the relationship between vessel dimensions and structure it is conventional to partition the vessels based on an ordering principle (see for example[1]). An ordering principle is a means of relating a given vessel to the overall architecture, typically using a metric for the extent of the structure proximal to that vessel. These metrics may be based purely on topology, as in Strahler ordering,[23] or include vessel properties as in diameter defined Strahler[1] and more recently volume ordering.[24]

For this work we use Strahler ordering[23] to partition the vessels. In this scheme, all of the segments that are leaves of the tree structure (the fine ends of the network) are assigned an order of one. At a bifurcation in which the order of the two daughter vessels are the same, the parent vessel segment is assigned an order one greater. At a bifurcation in which the order of the daughters differ, the parent is assigned the larger of the two orders. We define a vessel element[1] as a connected set of vessel segments of the same order. It follows from the definition that a vessel element will always be a series of one or more vessel segments. Element diameters are defined as the mean diameter along the segments making up an element and element lengths are defined as the sum of the lengths of these segments. A consequences of analyzing vessel elements is that fine off-shoots from a large vessel, which are typically of lower order, are unlikely to divide the large vessel into two vessel elements. This means that element length is less susceptible to noise than segment length.

A difficulty with an ordering rule starting from the leaves of the tree is that the capillaries which are the true first order vessels cannot be resolved by the micro-CT technique. For this work, we make the approximation that all of the vessel end points, which tend to be approximately 40 μm or two voxels in diameter, are of the same order.

2.5. Statistical analysis

As an illustration of the kinds of analysis made feasible by the methodology, we compared between specimens the distributions of both the vessel element diameters and vessel element lengths. Anticipating that the number of elements will increase geometrically as vessel dimensions decrease, these distributions were estimated using a histogram with a variable kernel or Parzen window size.[25] The kernels were normalized to removed the effect of kernel width on the distribution estimate.

3. RESULTS

3.1. Tubular model construction

Application of the spline approximation to all vessels in the vascular tree yields the results shown in Figure 5. Figure 5a is a segmentation of a kidney perfused with low viscosity contrast agent, 5b is the corresponding vessel skeleton following deletion of the arterial vessels, and 5c is the skeleton rendered as a tubular model. This is rendered by the implicit surface method with a sphere defined as each point on the vessel skeleton. Corresponding results shown in 5d, 5e, and 5f are the same steps for a kidney perfused with high viscosity contrast agent in which only the arterial vessels are visible. In general these are of smaller diameter than the corresponding vein, although arteries perfused with high viscosity contrast agent tend to be of larger caliber than arteries perfused with the low viscosity agent.

3.2. Comparing vessel dimensions

Histograms of element diameters computed are shown for arterial and venous vessels in Figure 6a and 6b respectively. These distributions are visually similar for the three specimens in both cases. A vessels of 40 μm diameter is two voxels wide on the micro-CT data. Vessels smaller than 40 μm tend to be lost during the segmentation and skeletonization procedures as reflected in the sharp drop off in element numbers below 40 μm.

A ramified vessel structure in which the vessel dimensions decrease geometrically in successive generations while the number of such vessels per generation increases exponentially is consistent with the relationship

$$p(d) = \beta_0 (d/d_0)^{\beta_1} \tag{2}$$

between element diameter d and the diameter density $p(d)$. For unit consistency, the constant d_0 is defined arbitrarily as $1\,mm$. Plotted with logarithmic scales on the axes, one can expect a linear relationship for the

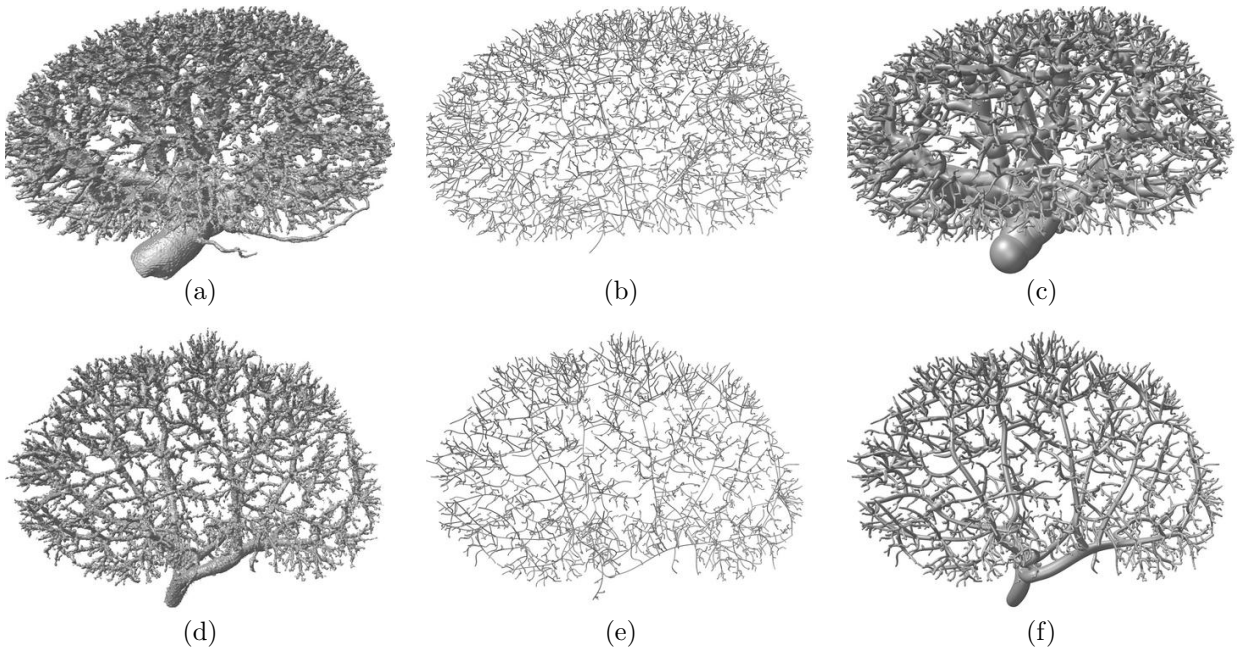

Figure 5. Vessel skeletonization and modeling of two kidney specimens. (a) segmented vessels for a low viscosity perfusion. (b) venous skeleton derived from *a*. (c) venous tubular model derived from *a*. (d) segmented vessels for a high viscosity perfusion. (e) arterial skeleton derived from *d*. (f) arterial tubular model derived from *d*.

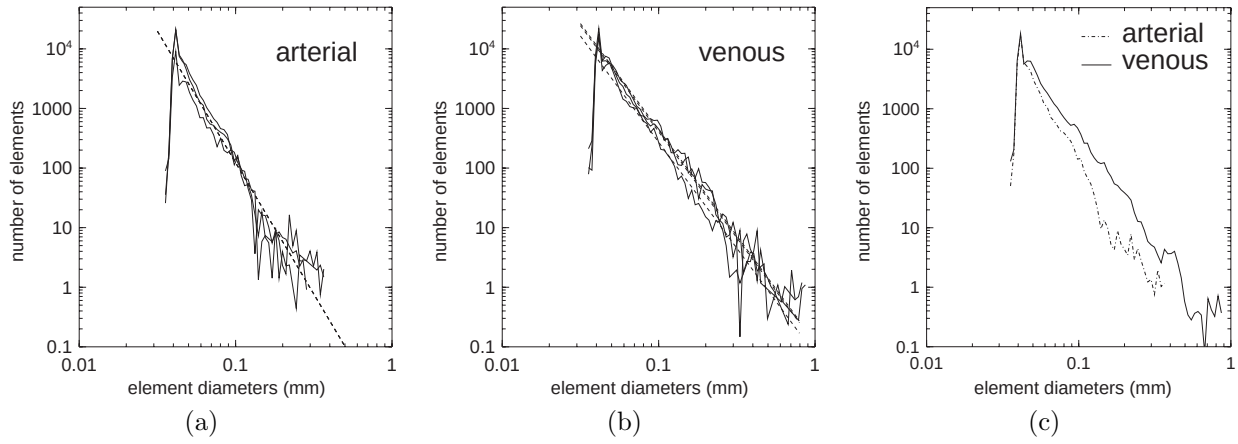

Figure 6. Histograms of vessel element diameters for each of the six specimens. Also shown are best fit lines describing the element density for diameters greater than 40 μm. (a) arterial distributions. (b) venous distributions. (c) averages of arterial and venous distributions.

Table 1. Regression coefficients for a linear fit of $\ln p(d)$ versus $\ln d$ for each specimen along with standard deviation estimates based on the residual fitting error.

	arterial			venous	
specimens	$\ln \beta_0$	β_1	specimens	$\ln \beta_0$	β_1
H1, H2, H3	-5.3 ± 0.7	-4.41 ± 0.12	L1, L2	-2.16 ± 0.4	-3.56 ± 0.05
			L3	-2.60 ± 0.4	

graphs shown in Figure 6. The best fit line for these cases, pooling data where appropriate, is also shown. The values of $\ln \beta_0$ and β_1 from linear regression of $\ln p(d)$ versus $\ln(d/d_0)$ are tabulated in Table 1. The standard deviations shown are estimated from the residual error in each case. Two analyses of covariance[26] were performed to test for differences between the slopes and offsets for the venous structures and arterial structures. At a threshold for significance of $p = 0.01$, no significant differences were found in the slopes among either the venous or arterial structures. The average slopes for the arterial and venous cases were $\beta_1 = -4.41 \pm 0.12$ and $\beta_1 = -3.56 \pm 0.05$ respectively.

Assuming homogeneous slopes, significant differences were observed in the offset $\ln \beta_0$ for the venous specimens, but not for the arterial structures. A post hoc Tukey's comparison of the individual venous structures indicated that specimen L3 differed from L1 and L2. Subtle differences in vessel diameter can be seen in Figure 1 in which the three specimens L1, L2, and L3 are shown in order. Given that all three distributions of $p(d)$ end with the renal vein on the right, the difference in β_0 should be interpreted as a shift of the distribution to the left. This corresponds to a 12% reduction in the diameter of corresponding vessels for case L3 as compared to the other two cases.

Histograms of vessel element length are shown in Figure 7 for the arterial and venous structures. These distributions do not show the linear relationship between $\ln p(l)$ and $\ln l$ that was observed for element diameters. As seen in Figure 7, the distribution of element lengths showed a high degree of consistency among specimens for the venous structure. While the arterial structure of specimens H1 and H2 are similar, specimen H3 shows a reduced number of short vessel elements. This is consistent with reduced numbers of fine vessels observed for this specimen. Comparing the average distributions for arterial and venous element lengths suggests considerable similarity (see Figure 7c). The degree of similarity between the two curves is remarkable given that arteries and veins are not strictly parallel in their layout.

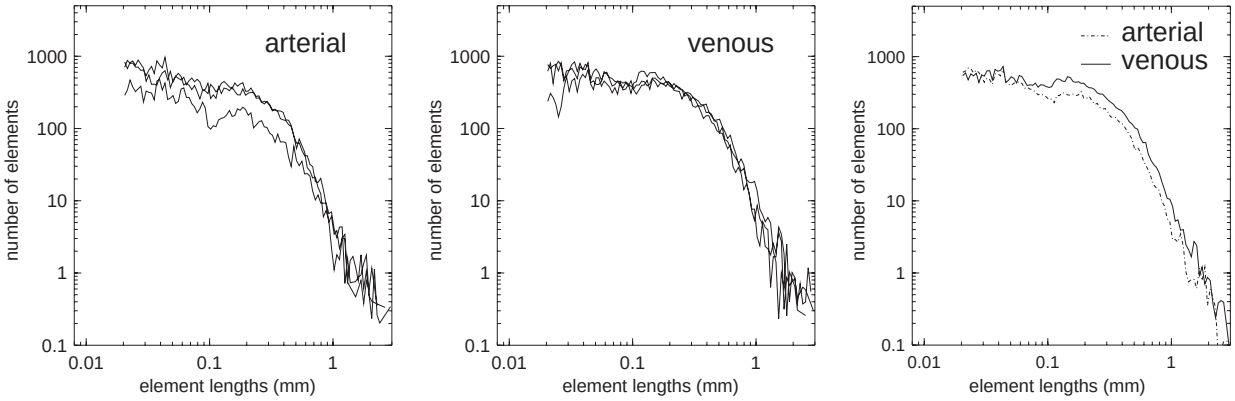

Figure 7. Histograms of vessel element lengths for each of the six specimens. (a) arterial distributions. (b) venous distributions. (c) averages of arterial and venous distributions.

4. DISCUSSION

We have described a complete method for assessment of microvascular structure including specimen preparation and statistical analysis. While individual steps in this procedure could be substituted by alternate methods, we have identified a number of features of this problem that all such methodologies should address. The first is the need to segment parallel touching vessels. Given the difficulty of perfusing only the venous side of the vasculature, veins are most easily identified retrospectively by image processing. Seen in cross section, an artery appears as a small disk adjacent to a larger disk. Moving along the vessel, the two disks shrink until the cusps in their combined cross section disappear and the two vessels can no longer be resolved. Resolution considerations mean that the number of arterial vessels that can be identified in the presence of the larger venous vessels is substantially less than are observed when only the arterial side is perfused. For this work, we did not retain the less detailed arterial tree in the fully perfused vasculature specimens and instead deleted the arterial network. In segmenting the vessels, it is not sufficient to treat a parallel artery and vein as a single unit since the two may separate and rejoin.

We have identified two cases in which arteries are difficult to segment from veins. The first is shown in Figure 3a in which the arteries and veins branch, continue to touch, but take on different topology. The algorithm described here produced the crossover connections shown in 3b between the artery and vein which had to be resolved manually. The second difficult case is a fine side branch off of a vein in which the side branch is too fine to resolve a corresponding arterial branch if one is present. As the new branch often touches the parent veins' arterial partner it is difficult for the segmentation procedure to distinguish this case from a branch in the artery although the later is less likely. Such cases requiring domain specific knowledge speak to the benefits of model based segmentation approaches employing deformable models[27,28]; however, the need to characterize these difficult cases in advance does not lend itself to an exploratory data analysis.

Another feature of segmenting microvasculature is that vessel diameters do not decrease monotonically as one moves from large to small vessels. Instead, vessels tend to be narrowest in the middle of a segment and thicken at a branch point. In cases where two branch points are nearby, this local thickening may exceed the long range thinning trend such that the average diameter of vessel segments also does not decrease monotonically. For this work we used the distance transform to define vessel diameter. This has the consequence that the diameters of vessels with elliptic cross sections are underestimated. However, this metric has the advantage that the diameter is defined for arbitrary cross sections and in otherwise ambiguous cases such as at branch points.

The third feature that must be addressed in segmenting microvasculature is the representation of short vessel segments. This is related to the handling of trifurcations. In general the point at which large vessels branch is difficult to estimate precisely. When two such branchings occur in close proximity, the trajectory of the connecting vessel segment is ill defined unless the surrounding context is taken into account. This is addressed by the principal vessel graph representation as one branch of every bifurcation is considered the continuation of the parent vessel. The PVG representation also allows for the vessel trajectories to be regularized and has the effect that the trajectory of a large vessel is not deflected by closely spaced fine branches. A feature of the PVG is that trifurcations are represented as coincident bifurcations connected by a zero length segment with a defined trajectory thus avoiding a syntactic distinction between close bifurcations and trifurcations.

The criteria used to determine which branch is the continuation of the parent vessel is the diameters of the daughter segments at the ends approaching the junction. Given that these diameter measurements tend to be less precise than those determined by subsequent spline approximation, the segment diameter d_2 may occasionally exceed d_1. In principle one could iteratively construct the PVG by reselecting the continuing vessels given the new diameter estimates. However, since only 5% of bifurcations had $d_1 < d_2$ and 90% of these were cases where the two daughters had equal Strahler order, we did not perform this relabelling.

The comparison results presented in section 3.2 provide a form of validation of the overall robustness and consistency of the measurement technique although the variability observed is a mixture of the measurement precision as well as natural anatomical variation that is present even in in-bred animals. The distribution of diameters was found to be well approximated by a power law relationship between the number of vessel elements and the vessel diameter with no significant differences in the exponent β_1 among either the venous or arterial structures. A significant difference β_0 was noted for one of the venous structures. We interpret this as that

sample having a 12% reduction in the size of vessels the same frequency of occurrence. Another difference that was noted was a reduction in the number of short length elements in one of the arterial samples. The perfusion methodology is the likely source of both these differences.

Assuming a parallel structure between arterial and venous vessels, the differing exponents for the diameter distribution, -4.43 for arterial and -3.56 for venous, can be interpreted as a more rapid decrease in the diameter of veins with successive bifurcations. A linear form to the distribution of vessel element lengths was neither anticipated nor observed. In choosing to measure elements rather than segments, the intent was to define a fundamental vessel unit whose properties could be robustly measured in the presence of both instrument noise and a wide range of vessel dimensions. While the arterial and venous networks were observed to have similar structure, the arteries being smaller means that fewer arterial segments are observed. The degree of similarity between the arterial and venous distributions of element length suggests that the partitioning strategy is effective at reducing this bias.

5. CONCLUSIONS

Micro-computed tomography provides a means for obtaining a detailed three-dimensional description of the structure of micro-vasculature in whole organs. In combination with the powerful techniques that are available for manipulation of experimental mice, this technique provides a means to address questions about the role of microvascular structure in disease and development. The use of a 3D imaging technique for this problem shifts the methodological burden from that of data collection, which is relatively rapid with micro-CT, to one of image segmentation and analysis. In this paper we have identified the main challenges presented by such analysis and described a semi-automated method for analysis of kidney microvasculature. In particular, we have described a method for segmentation of parallel arteries and veins as well as a structural decomposition that facilitates regularization of complex vascular structures. The combination of specimen preparation, micro-CT imaging and this analysis procedure is shown to provide consistent results among animals of the same strain with precise distributions of vessel diameter, vessel length, and branching angles for both arterial and venous vasculature.

ACKNOWLEDGMENT

This work was supported by the Canadian Institutes for Health Research and the National Cancer Institute of Canada.

REFERENCES

1. G. S. Kassab, C. A. Rider, N. J. Tang, and Y. C. Fung, "Morphometry of pig coronary arterial trees," *American Journal of Physiology* **265**, 1993. (Heart Circulation Physiology 34).
2. C. D. Murray, "The physiological principle of minimum work: I. the vascular system and the cost of blood volume," *Proceedings of the National Acadamy of Sciences USA.* **12**, pp. 207–214, 1926.
3. C. D. Murray, "The physiological principle of minimum work applied to the angle of branching of arteries," *Journal of General Physiology* **9**, pp. 835–841, 1926.
4. D. L. Cohn, "Optimal systems I. the vasular system," *Bulletin of Mathematical Biophysics* **16**, pp. 59–74, 1955.
5. M. Zamir, "Optimality principles in arterial branching," *Journal of Theoretical Biology* **62**, pp. 227–251, 1976.
6. S. Rossitti and J. Löfgren, "Vascular dimensions of the cerebral arteries follow the principle of minimum work," *Stroke* **24**(3), pp. 371–377, 1993.
7. W. Schreiner and P. F. Buxbaum, "Computer-optimization of vascular trees," *IEEE Transactions on Biomedical Engineering* **40**, pp. 482–490, 1993.
8. V. V. Gafiychuk and I. A. Lubashevsky, "On the principles of the vascular network branching," *Journal of Theoretical Biology* **212**, pp. 1–9, 2001.
9. R. W. Glenny and H. T. Robertson, "A computer simulation of pulmonary perfusion in three dimensions.," *Journal of Applied Physiology* **79**(1), pp. 357–369, 1995.

10. D. A. Beard and J. B. Bassingthwaighte, "Fractal nature of myocardial blood flow emerges from whole-organ model of arterial network," *Journal of Vascular Research* **37**(4), pp. 282–296, 2000.
11. S. M. Jorgensen, O. Demirkaya, and E. L. Ritman, "Three-dimensional imaging of vasculature and parenchyma in intact rodent organs with x-ray micro-ct," *American Journal of Physiology* **275**, pp. H1103–H1114, 1998.
12. M. D. Bentley, M. C. Ortiz, E. L. Ritman, and J. C. Romero, "The use of microcomputed tomography to study microvasculature in small rodents," *American Journal of Physiology* **282**, pp. R1267–R1279, 2002.
13. M. Marxen, M. M. Thornton, C. B. Chiarot, G. Klemen, J. Koprivnikar, J. G. Sled, and R. M. Henkelman, "Micro ct scanner performance and considerations for vascular specimen imaging," *Medical Physics* **31**(2), pp. 305–313, 2004.
14. S.-Y. Wan, A. Kiraly, E. Ritman, and W. Higgins, "Extraction of the hepatic vasculature in rats using 3-d micro-ct images," *IEEE Transactions on Medical Imaging* **19**, pp. 964–971, 2000.
15. L. A. Feldkamp and J. W. Kress, "Practical cone-beam algorithm," *Journal of the Optical Society of America* **1**(6), pp. 612–619, 1984.
16. R. Adams and L. Bischof, "Seeded region growing," *IEEE Transactions on Pattern Analysis and Machine Intelligence* **16**(6), p. 647, 1994.
17. Y. Zhou and A. W. Toga, "Efficient skeletonization of volumetric objects," *IEEE Transactions on Visualization and Computer Graphics* **5**(3), pp. 196–209, 1999.
18. J. C. Chato, "Heat transfer to blood vessels," *Journal of Biomechanical Engineering* **102**(2), pp. 110–118, 1980.
19. L. Zhu, "Theoretical evaluation of contributions of heat conduction and countercurrent heat exchange in selective brain cooling in humans.," *Annals of Biomedical Engineering* (3), pp. 269–277, 2000.
20. D. MacDonald, "MNI Display v1.3," 2002. [Online]: `http://www.bic.mni.mcgill.ca/software/`
21. P. Dierckx, *Curve and Surface Fitting with Splines*, Monographs on Numerical Analysis, Oxford University Press, 1993.
22. P. Dierckx, "DIERCKX," 1993. [Online]: `http://www.netlib.org/dierckx/`
23. A. Strahler, "Quantitative analsis of watershed geomorphometry," *Trans. Am. Geophys. Un.* **38**, pp. 913–920, 1957.
24. M. Marxen and R. M. Henkelman, "Branching tree model with fractal vascular resistance explains fractal perfusion heterogeneity," *American Journal of Physiology* **284**, pp. H1848–H1857, 2003.
25. R. O. Duda and P. E. Hart, *Pattern Classification and Scene Analysis*, John Wiley, 1973.
26. J. H. Zar, *Biostatistical Analysis*, ch. 18, pp. 369–371. Prentice Hall, New Jersey, 4th ed., 1999.
27. T. McInerney and D. Terzopoulos, "Topology adaptive deformable surfaces for medical image volume segmentation," *IEEE Transactions on Medical Imaging* **18**(10), pp. 840–850, 1999.
28. S. Aylward and E. Bullitt, "Initialization, noise, singularities, and scale in height-ridge traversal for tubular object centerline extraction," *IEEE Transactions on Medical Imaging* **21**(2), pp. 61–75, 2002.